CHALMERS
UNIVERSITY OF TECHNOLOGY

Universal Capacitance Boost—Smart Surface Nanoengineering by Zwitterionic Molecules for 2D MXene Supercapacitor

Universal capacitance boost – Smart surface nanoengineering by zwitterionic molecules for 2D MXene supercapacitor

Lukáš Děkanovský,*[a] Jalal Azadmanjiri, [a] Martin Havlík, [b] Pal Bhupender, [a] Jiří Šturala, [a] Vlastimil Mazánek, [a] Alena Michalcová, [c] Lunjie Zeng, [d] Eva Olsson, [d] Bahareh Khezri,*[a] Zdeněk Sofer*[a]

[a] L. Děkanovský, Dr. J. Azadmanjiri, Dr. P Bhupender, Dr. J. Šturala , Dr. V. Mazánek , Dr. B. Khezri, Prof. Dr. Z. Sofer
Department of Inorganic Chemistry, University of Chemistry and Technology Prague, Technická 5, 166 28 Prague 6, Czech Republic
E-mail: zdenek.sofer@vscht.cz, bahareh.khezri@vscht.cz, dekanovl@vscht.cz
[b] Dr. M. Havlík
Department of Analytical Chemistry, University of Chemistry and Technology Prague, Technická 5, 166 28 Prague 6, Czech Republic
[c] Dr. A. Michalcová
Central Laboratories, University of Chemistry and Technology Prague, Technická 5, 166 28 Prague 6, Czech Republic
[d] Dr. L. Zeng, Prof. E. Olsson
Department of Physics, Chalmers University of Technology, Fysikgränd 3, 412 96 Gothenburg, Sweden

Abstract: Two-dimensional (2D) nanomaterials, as one of the most widely used substrates for energy storage devices, have achieved great success in terms of the overall capacity. Despite the extensive research effort dedicated to this field, there are still major challenges concerning capacitance modulation and stability of the 2D materials that need to be overcome. Doping of the crystal structures, pillaring methods and 3D structuring of electrodes have been proposed to improve the material properties. However, these strategies are usually accompanied by a significant increase in the cost of the entire material preparation process and also a lack of the versatility for modification of the various types of the chemical structures. Hence in this work, versatile, cheap and environmentally friendly method for the enhancement of the electrochemical parameter of various MXene-based supercapacitors (Ti_3C_2, Nb_2C and V_2C), coated with functional and charged organic molecules (zwitterions – ZW) is introduced. The MXene-organic hybrid strategy significantly increases the ionic absorption (capacitance boost) and also forms a passivation layer on the oxidation-prone surface of the MXene through the covalent bonds. Therefore, this work demonstrates a new, cost-effective, and versatile approach (MXene-organic hybrid strategy) for the design and fabrication of hybrid MXene-base electrode materials for energy storage/conversion systems.

Introduction

Growing concerns related to the quality of the environment and the pursuit of carbon neutrality require society to move towards sustainable and renewable resources. The rapid development of renewable energy sources in the past decade has led to the development of energy storage systems to handle electricity. Consequently, electrochemical energy storage devices including batteries, fuel cells and electrochemical capacitors (ECs) have received great attention to fulfil this quest.[1]

In general, the energy and power density of any energy storage device is grounded by the fundamental charge storage mechanism and the relevant kinetic parameters at the electrode-electrolyte interface. For example, batteries can provide reversible redox reactions that include intercalations of mobile metal ions into the bulk structure of the electrode material. This process is accompanied by high energy densities, while the power density is missing. In comparison, the electrochemical double-layered capacitors (EDLCs), which can be called supercapacitors, provide high power densities, long cycle lifetimes, and fast charge-discharge abilities. These advantages allow supercapacitors to be complementing batteries for high-power applications. The distinct power density of the EDLCs is related to the charge storage mechanism. EDLCs store the charge only on surfaces (in contrast to batteries), so their availability is not limited by diffusion processes, allowing high power to be achieved. [2] Typically, EDLCs store charge on the interface of the electrode and electrolyte (electrode surface) through electrostatic absorption without charge transfer. Therefore, the surface area for electrolyte ions limits the capacity of the EDCLs. In this regard, pseudocapacitive materials, such as conductive polymers and various metal oxides can be a promising replacement for conventional materials. As these materials provide fast reversible surface redox reactions, the energy density comparable to batteries is achievable and the high power densities can also be maintained.[3] The basic requirements of a suitable material for energy storage applications are a) high conductivity and surface area, b) modulation of the capacitance by redox reaction and c) suitable surface functionalization.

2D nanomaterials are classified as ideal candidates for energy storage applications due to their high surface area and unique electrical, mechanical, and optical properties. To date, graphene, MoS_2, phosphorene, and their derivatives[4] are among the most explored materials in this field that have shown promising results. On the other hand, many novel 2D materials have been synthesized in recent years such as hexagonal boron nitrides,[5] transition metal dichalcogenides,[6] silicene,[7] germanane[8] or metal oxides[9]. All of these can find broad application potential in optoelectronics, biology, medicine, environmental protection, catalysis, sensors, energy storage, and conversion.[10] More recently, a new broad family of 2D transition metal carbides and nitrides (MXenes), have shown great perspective in pseudocapacitive energy storage applications.

MXenes meet all the requirements for being ideal candidates, as they have highly reversible surface redox reactions, great conductivity and considerable surface area.[11] Traditionally, MXenes have been synthesized by ternary layered materials (MAX phases). MAX phases are generally represented by $M_{n+1}AX_n$ (n is an integer between 1 and 4) the formula, where M represents transition metal (such as Ti, V, Nb, Mo, Cr), A is an element from 13 or 14 groups in the periodic table (Al, Si, Ga or

In) and X represents carbon or nitrogen.[12] Synthesis of MXenes from MAX phases requires selective etching of the A element using an acid (hydrofluoric acid (HF)). The resulting formula is then $M_{n+1}X_nT_x$, where T_x represents surface functional groups (-OH, -F or -O), which govern the final functional performance for the electrolyte/electrode interaction.[13] The unique layered structure and properties of MXenes bring considerable attention to this family of materials, especially for energy storage applications. These unique properties can be summarized as 1) the transition metal carbide core is characterized by metallic conductivity, which provides considerable electron transfer through the structure of the material;[14] 2) the transition metal oxide surface behaves like a redox-active center for interaction with electrolyte[11] and 3) the surface functional groups allow us to modify the resulting surface appropriately.[15] One of the most common and studied materials up to date from the MXene family is $Ti_3C_2T_x$, which was discovered in 2011 by Drexel scientists.[13] Titanium carbide ($Ti_3C_2T_x$) has recently come to the forefront of interest in many applications, including metal-ion batteries, supercapacitors and capacitors.[16] $Ti_3C_2T_x$ is characterized by its high metallic conductivity (up to 8000 S cm^{-1})[17] that together with the redox centers on the surface and the functionalization group providing the most striking features of $Ti_3C_2T_x$. However, symmetric $Ti_3C_2T_x$ MXene-based supercapacitor devices usually show limited operating voltage windows (~0.6 V). $Ti_3C_2T_x$ is considered an oxidation-prone material at higher anodic potentials.[18] Despite the enormous research efforts and undoubtedly properties of this material, there are still limiting factors that restrict its applications such as 1) material stability in various environments (electrolytes); 2) layering of the material caused by the influence of Van der Walls interactions (it limits the active surface area for charge adsorption); 3) limitation in large-scale production of the material and 4) oxidation-prone property. Consequently, many efforts have been made to improve the material-electrode design and electrochemical performance of supercapacitors, such as i) coating thickness design; ii) microporous electrode design; iii) pillaring of individual 2D layers; iv) redesign of surface functional groups; and v) doping, modulate the electrochemical properties of MXene based supercapacitors.
As the layer thickness increases, the number of electrochemical active redox sites available on the surface of the material will decrease and consequently, the capacitance will be reduced. An enhancement will also occur in ionic resistivity due to the diffusion mechanisms. The novel electrode engineering and design can overcome these challenges. Tingting Tu et al. have designed a 3D electrode based on hydrogels.[19] This 3D design significantly improved the availability of the active sites, demonstrating that the electrode architecture is a highly effective strategy to improve the electrochemical properties of supercapacitors. The 3D design has also increased the porosity and shortened the distance required for ion transfer compared to conventional 1/2D structures. Currently, the most common electrode design is being developed using template-assisted methods, 3D printing or electrospinning to create nanofiber textures.[10] An excellent example of material nanostructure modification is the pillaring technique. This technique is generally used to increase the individual distance between 2D layers of materials. It works according to the intercalation of the surfactant molecules (e.g. CTAB) with the materials, which increases the interlayer distance. As a result, the number of electroactive sites enhances. It is also possible to design the layer spacing in such a way as to suit the intercalated ion. Luo et al. have employed this method and increased the original spacing of 0.977 nm to 2.708 nm (177%). [20] Another common strategy to improve the electrochemical performance of electrode materials is doping. The doping of the MXene crystal lattice has shown a significant effect on the final charge transport through the structure, and the electrochemical redox processes can also be modulated. Garg et al. studied the effect of Vanadium doping on Ti_3C_2 MXenes and an accelerated charge transport was observed.[21] Despite all these advances, it is essential to come up with new alternatives that can make suitable materials for supercapacitors in one synthetic step. The challenge is to find a simple and universal method for various materials to enhance their final electrochemical performances.
One of the promising solutions to overcome this challenge would be an MXene-organic hybrid design. This design could be based on grafting the materials with functional and charged organic molecules (zwitterions - ZW). This unique nanoarchitecture of the surface of the material, along with π-π stacking, would be an advantage for ionic transport and electrochemical storage applications.[22] Furthermore, this procedure increases the stability of the material and also the ionic absorption (from the electrolyte environment).[23] Although the original nature of the pristine material remains the same, surface functionalization of MXenes and the reactivity of the charged organic molecules will significantly improve the electrochemical storage property.
Herein, we focus on our hypothesis of the multifunctional usage of ZW as an optimal surface modulator to alter the electrochemical parameters of the supercapacitors for various MXenes. We synthesized different MXenes, including $Ti_3C_2T_x$, Nb_2CT_x and V_2CT_x (**Scheme 1A**), which were coated by a one-step and scalable synthetic procedure using ZW (**Scheme 1B**). In this step, benefiting from the oxygen-containing functional groups on the surface of the MXenes and ethoxy groups on the ZW, a covalent bond (MXene-ZW) is formed through condensation. Such important interfacial compatibility fulfils the requirements for energy storage applications while preserving the original redox functionality and accessibility of the ions in the electrolyte. In addition, mesoporous -Si-O-Si- forms a passivation layer to enhance material stability. The final density of the ZW coating has been changed by varying the hydrolytic condensation process (up to 1, 2, 4 and 8h). The resulting materials are mixed with polyvinylidene fluoride (PVDF, binder) and N-Methyl-2-

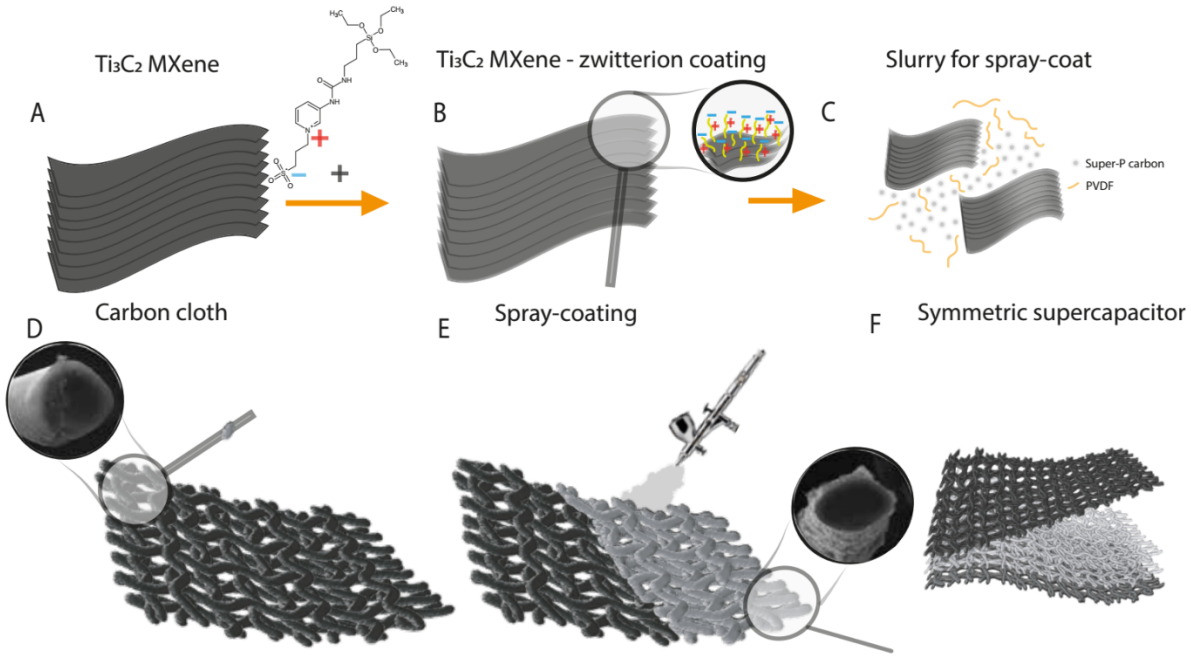

Scheme 1. Schematic illustration of the symmetric supercapacitor preparation: A) Preparation of the MXene; B) Modification of the MXene by a thin coating of ZW; C) Slurry formation; D) Pristine carbon cloth; E) Spray coating of the active material on the carbon cloths; F) Assembling of the symmetric supercapacitor.

pyrrolidone (NMP, solvent) to make a slurry for spray coating (**Scheme 1C**). To achieve a 3D structured electrode design, a flexible carbon cloth was employed and sprayed with prepared slurry (**Scheme 1D**). It resulted in a homogeneous core-shell structure of carbon fibres/ MXene-ZW (**Scheme 1E**). Finally, a symmetric supercapacitor was assembled using cellulose separators for the electrochemical test (**Scheme 1F**).

Results and Discussion

To design a suitable and multifunctional coating material for energy storage, the interfacial compatibility and final structure of MXene-organic hybrids need to be considered. The charged end of the molecules can form an additional sorption layer for electrolyte ions, while, simultaneously, accessibility of the ions to the pristine MXene surface should be preserved. As an example, the initial MAX phase Ti_3AlC_2 (structure represented by **Scheme 2A**) works as a precursor for the final Ti_3C_2 MXene (**Scheme 2B**). The surface layers contain oxygen functional groups, which are used for covalent attachment with ZW molecules. The ZW molecules were synthesized by a two-step process (schematic illustration of an intermediate and final molecule called Silan A and Silan B (**Scheme S1-A+B**) with detailed NMR and MS characterization (see **Figure S1+2** with their corresponding description in SI). The Si-OEt groups on the ZW will be hydrolysed to form a Si-OH structure as a result of the so-called hydrolytic condensation process. Later, Si-OH groups either undergo a dehydration condensation reaction to form oligomers or remain covalently attached to the MXene surface (**Scheme 2C**).[24] Final functionality provides enhanced ion absorption while preserving the pristine surface and continues to provide sufficient space for ions to penetrate on the MXene surface as well (**Scheme 2D**). In optimal conditions, a significant increase in the resulting capacitance will be expected. This increase is a function of the coverage density of ZW on the surface (**Scheme 2E**).

Thermogravimetric (TG) and X-ray diffraction (XRD): thickness/density optimization study

TG analysis was performed in Ar/O_2 atmosphere (4:1) to prove the successful ZW coating on the MXene surface and quantify the increase in ZW density by varying the hydrolytic condensation process (1, 2, 4 and 8 h). It can also verify the prediction of MXene passivation before oxidation, resulting in mesoporous -Si-O-Si- structure formation. As can be seen in **Figure 1A**, the weight change for the pristine Ti_3C_2 MXene can be divided into three phases. The weight loss phase starts at room temperature (RT) to 280 °C. In this phase, the bonded water and HF are released. The first phase reaches an approximately weight loss of 6 %. The second phase starts at 290 °C to 470 °C and shows a mass increase of 13% that could be the result of the oxidation of MXene. Lately, the decomposition phase has been observed.[25] In comparison, after the hydrolytic condensation of Ti_3C_2 MXene with ZW molecules, the MXene oxidation will occur at higher temperatures (365 °C (1h), 378 °C (2h), 381 °C (4h) and 386(8h)). The weight loss increases from 9% (1h) to 11% (2h), 12.5% (4h) and 14% for 8 hours of reaction. These results confirm the successful immobilization of ZW molecules into the MXene and the gradual increase in ZW density on the surface as a function of hydrolytic condensation reaction time. Simultaneously, we observe prolonged preservation of the MXene surface against oxidation after coating.

The crystal structure was studied using XRD analysis (**Figure 1B**). The most significant structural pattern for pristine Ti_3C_2 MXene has a crystalline nature, and the 2Θ peak at 9.3° (002) is a characteristic peak of the interplanar crystal spacing of 12.46 Å.[26] In addition 2Θ peaks at 18.6° (006), 27.9° (008), 34.6° (102), 36.9° (103), 46.9° (107), 61.1° (110) and 72.5° (118) confirm the crystalline nature of the MXene and the occurrence of the etching process. The peak position and width remain constant

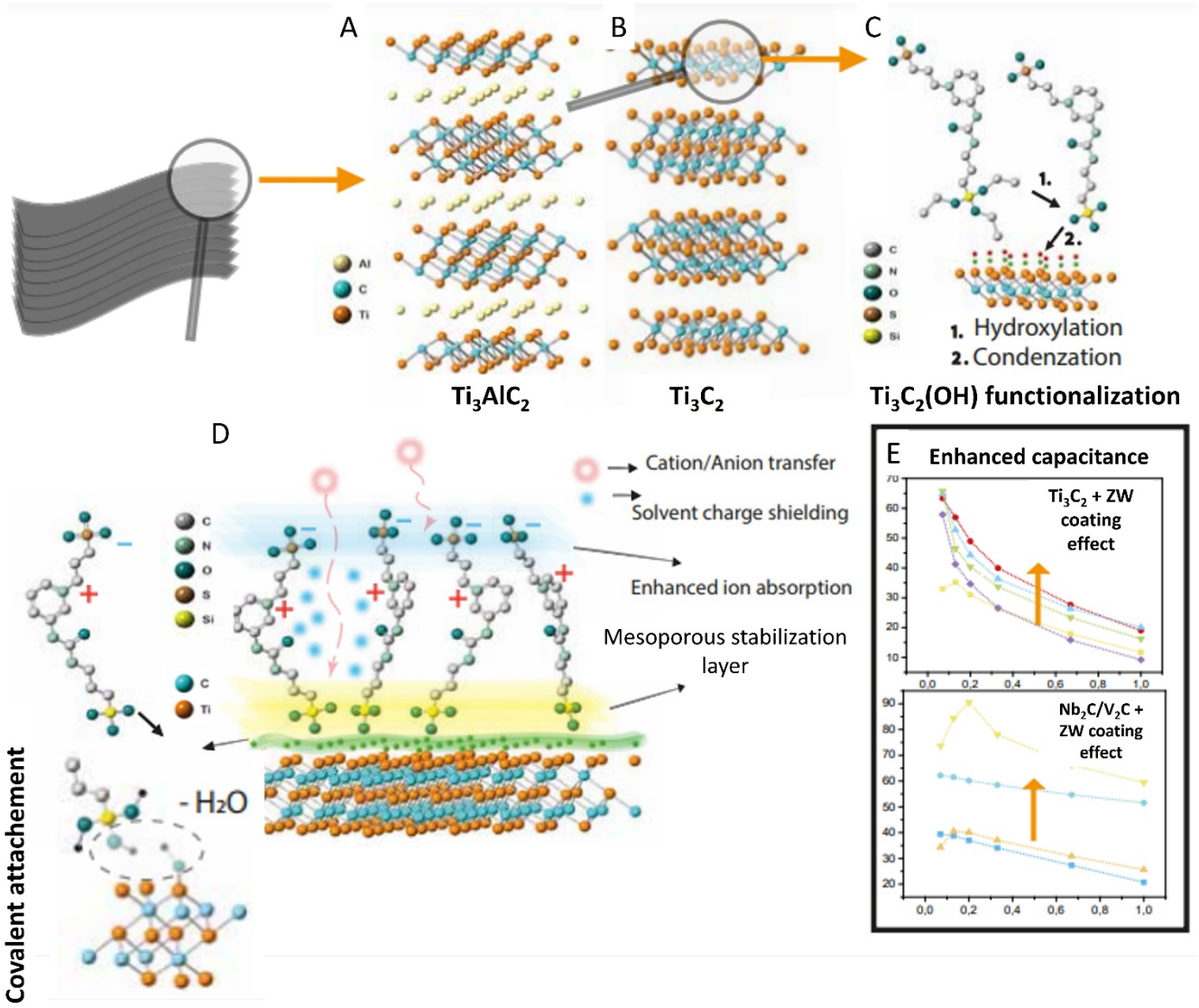

Scheme 2. Schematic demonstration of the MXene nanoengineering by thin ZW coating and resulting electrochemical effect: A) Pristine MAX phase of Ti_3AlC_2; B) Ti_3C_2 MXene structure; C) Covalent attachment of the ZW on the MXene by subsequent hydroxylation and condensation; D) Functional coating that forms a mesoporous stabilization layer and enhanced ion absorption, while maintaining ion transfer to the MXene surface; E) Final capacitance enhancement caused by ZW coating.

after the hydrolytic condensation process (coating with ZW molecules). Because of the presence of the ZW molecules (amorphous phase) on the surface of MXene, the intensity of the significant MXene peaks gradually lessened as the hydrolytic condensation time increased. Accordingly, the presence of the ZW molecules on the surface of the MXene layers can be proved; given the steric and charge barriers, its intercalation into individual layers is difficult. Similar conclusions can also be found in the case of the analysis of Nb_2C and V_2C materials before and after ZW coating (**Figure S3A)**, which are described in more detail in SI.

FTIR and Raman analysis

FTIR analysis was performed before and after ZW coating for a detailed evaluation of the surface functionalization of Ti_3C_2 MXene (**Figure 1C**). As can be seen, corresponding -OH and C-F vibrations at 3377 cm^{-1} and 922 cm^{-1}, respectively, provide us with information on the surface functionalization of the material. Especially, the -OH terminating groups play a significant role in the covalent attachment of the ZW molecules and are very advantageous for this type of modification. We can also observe the overlapped signals belonging to C-H at ~3000 cm^{-1} and an intensive vibration at 1514 cm^{-1}.[27] After modification with ZW molecules, C=O stretching frequency N-H stretching and deformation frequencies appear at 1736 cm^{-1}, 3455 cm^{-1} and 1641 cm^{-1}, respectively. The C-N stretching frequency occurs at 1446 cm^{-1}. The broad -OH and aromatic ring vibrations have been observed at 3251 cm^{-1} and 3022 cm^{-1}, respectively. There are also significant vibrations at 1375 cm^{-1} (S=O) and 1098 cm^{-1} with 909 cm^{-1} that are the index of the formed Si-O-Si and Si-O-Ti bindings. The Si-O-Ti linkage stretching bond allows us to confirm the successful covalent anchoring of ZW molecules to the MXene surface.[28]

Raman spectra of pristine carbon fibres coated as the final electrode were collected to evaluate successful coverage and has been compared with carbon clothes and Ti_3C_2 as blanks (**Figure 1D**). The carbon cloth textile (substrate, red line) exhibits two prominent Raman bands, the G-line which corresponded to the Raman-allowed E_{2g} vibrational mode, and the D-line corresponded to disorder-induced lines (1653 and 1386 cm^{-1}).[29] Pristine Ti_3C_2 MXene shows all characteristic peaks at 706, 623, 375 and 213 cm^{-1}. Peaks at 213 cm^{-1} and 706 cm^{-1} are assigned to Ti-C and C-C vibration mods of oxygen terminated Ti_3C_2

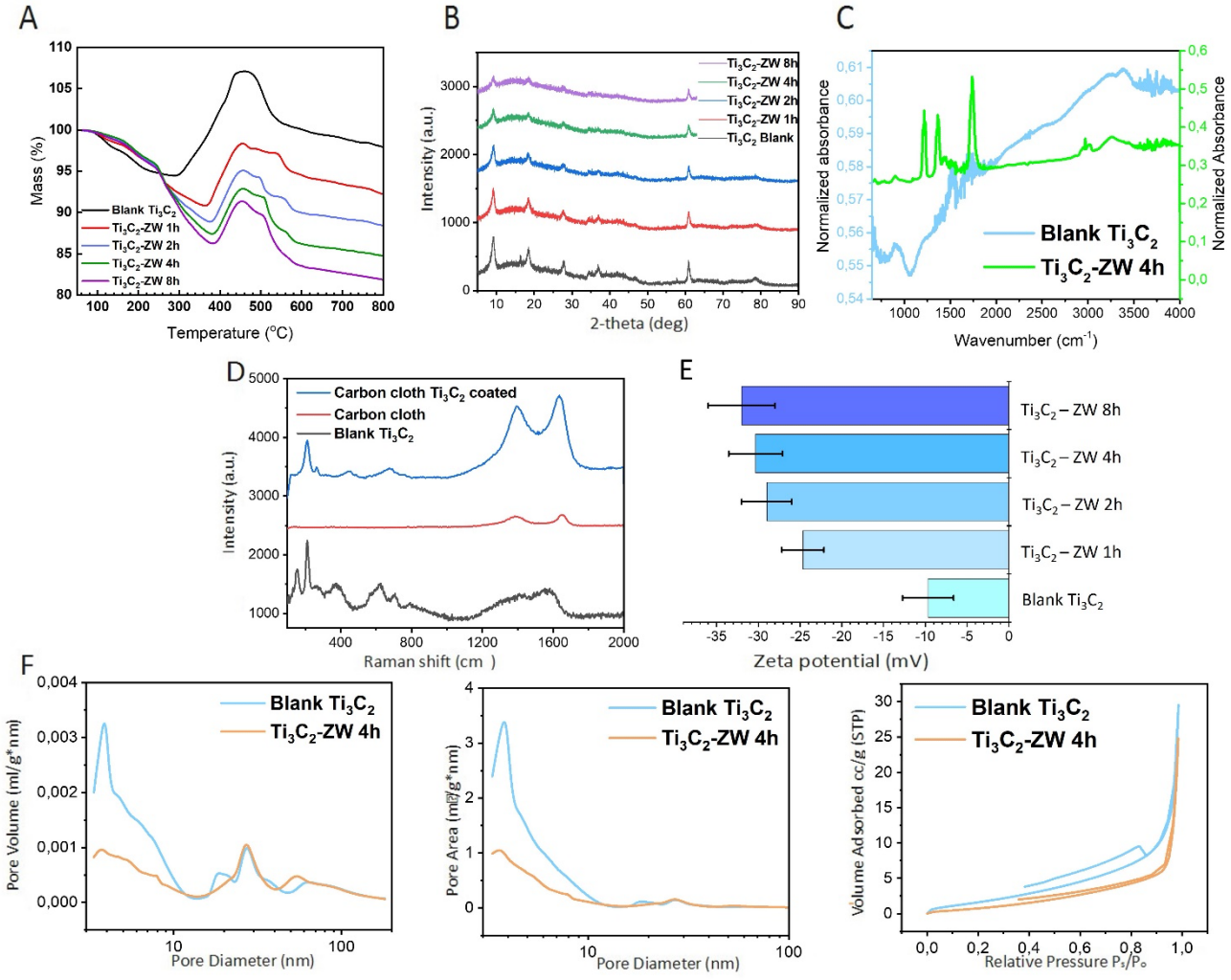

Figure 1. Material characterization of the active MXene-ZW material: A) TG analysis of the pristine Ti_3C_2 MXene and the final ZW coated composites after different reaction times (1,2,4 and 8h); B) XRD analysis of the pristine T_3C_2 MXene and final ZW coated composites after different reaction times (1,2,4 and 8h); C) FTIR analysis of the pristine Ti_3C_2 before and after ZW coating; D) Raman spectra up to the final electrode structure covered with MXene-ZW active material; E) Zeta-potential analysis of the pristine TI_3C_2 MXene and the final ZW coated composites after different reaction times (1,2,4 and 8h); F) BET analysis of the pristine Ti_3C_2 MXene before and after coating with ZW (4h reaction time).

MXenes. The peak at 375 cm^{-1} is attributed to the Ti-O peak at 623 cm-1 which mainly indicates the non-stochiometric TiC_x or C-O vibrations. Usually, the sharp peak at 153 cm^{-1} occurs in incomplete etched MXenes with Al residues. The observed signals at 1567 cm^{-1} and 1383 cm^{-1} correspond to disordered graphite structures and defects.[30] These results confirm the presence of functional groups such as -OH or -O on the surface of the MXene, as previously found by FTIR. The spray-coated carbon cloths show a combined signal, dominated by the characteristic of graphitic carbon broadband, which is used in the spray-coating procedure. The observations show that no oxidation occurs during material preparation and the resulting active material incorporated into the 3D structure of the electrode is stable. The relevant analytical signals for Nb_2C and V_2C MXenes are given in **Figure S3B**.

Zeta-potential, BET analysis and STEM-EDS and EELS analysis

To prove the orientation of ZW molecules on the surface of MXene materials, Zeta analysis was performed (**Figure 1E**). The results show the orientation of ZW molecules on the MXene surface in the following arrangement: 1) the Si-OH end of the ZW molecules is involved in a covalent interaction with -OH functional groups on the Ti_3C_2 surface; and 2) sterically non-hindered SO^{3-} ends can freely orient into space and interact with the electrolyte. As can be seen, a Zeta-potential rapidly decreases to minus values (from -10 mV for pristine Ti_3C_2 to -25 mV and then -30 mV

as the hydrolytic condensation reaction progresses). An analogous measurement was also performed for Nb_2C and V_2C MXenes before and after ZW coating (**Figure S3C**). It should be noted that the change in the absolute value of the zeta potential varies for different types of MXenes before and after coating. Ti_3C_2 showed the highest change followed by Nb_2C and then V_2C, which corresponds to the final electrochemical performance of the electrodes. Those dropdowns to negative zeta-potentials significantly improve the attractivity of the ZW coated material surface for electrolyte ions and surface charge density becomes one of the most significant parameters.

As surface area plays an important role in final capacitance, the BET analysis was performed to evaluate the effect of ZW modification (see **Figure 1F**). As can be seen in the pore volume/Area distribution graphs, the hydrolytic condensation reaction results in the closure of the small pores of the MXene substrates by ZW molecules. The same trend has been observed for (Nb_2C and V_2C, as presented in **Figure S4**). This fact is in agreement with the decrease in the absorbed volume of N_2, showing the hysteresis graphs for all three MXenes. It is noteworthy to emphasize that despite the decreasing proportion of the small pores in the material, a significant improvement has been shown in their electrochemical characterization. The surface area occupied by the ZW molecules is expected to enable full binding to the charged electrolyte ions while protecting the oxidation-prone surface structures.

As shown in EELS and EDS analysis (**Figure 2)**, ZW molecules occupy primarily the sharp edges of the MXene flakes, without deep penetration to the crystal; consequently, they preserve MXene flakes against the oxidative influence of the environment and rapidly enhance the adsorption of charged ions. From the analysis of the ZW binding state (**Figure 2A** for pristine Ti_3C_2 and **Figure 2B** for ZW coated Ti_3C_2) we can observe clear Si-L signal indicating obvious Si-O bonding. The Si signal is strong and extends from ~104 eV to ~ 200 eV. S-L signal (~ 160 eV) is superimposed on the tail of the Si signal. The shape of the O signal indicates the existence of the Ti-O-Si bonding starting at ~ 530 eV. In **Figure 2C** we provided STEM-EDS maps showing the localization of the ZW coating, where the edges of the MXene flakes are primarily modified. The fact, we observe highest concentration of the Si signal from both EDS and EELS mapping, may be attributed to highest concentration of hydroxyl functional groups on the surface of the material. Oxide functional groups on the surface of the material allow us to achieve both covalent and electrostatic interactions under experimental conditions.

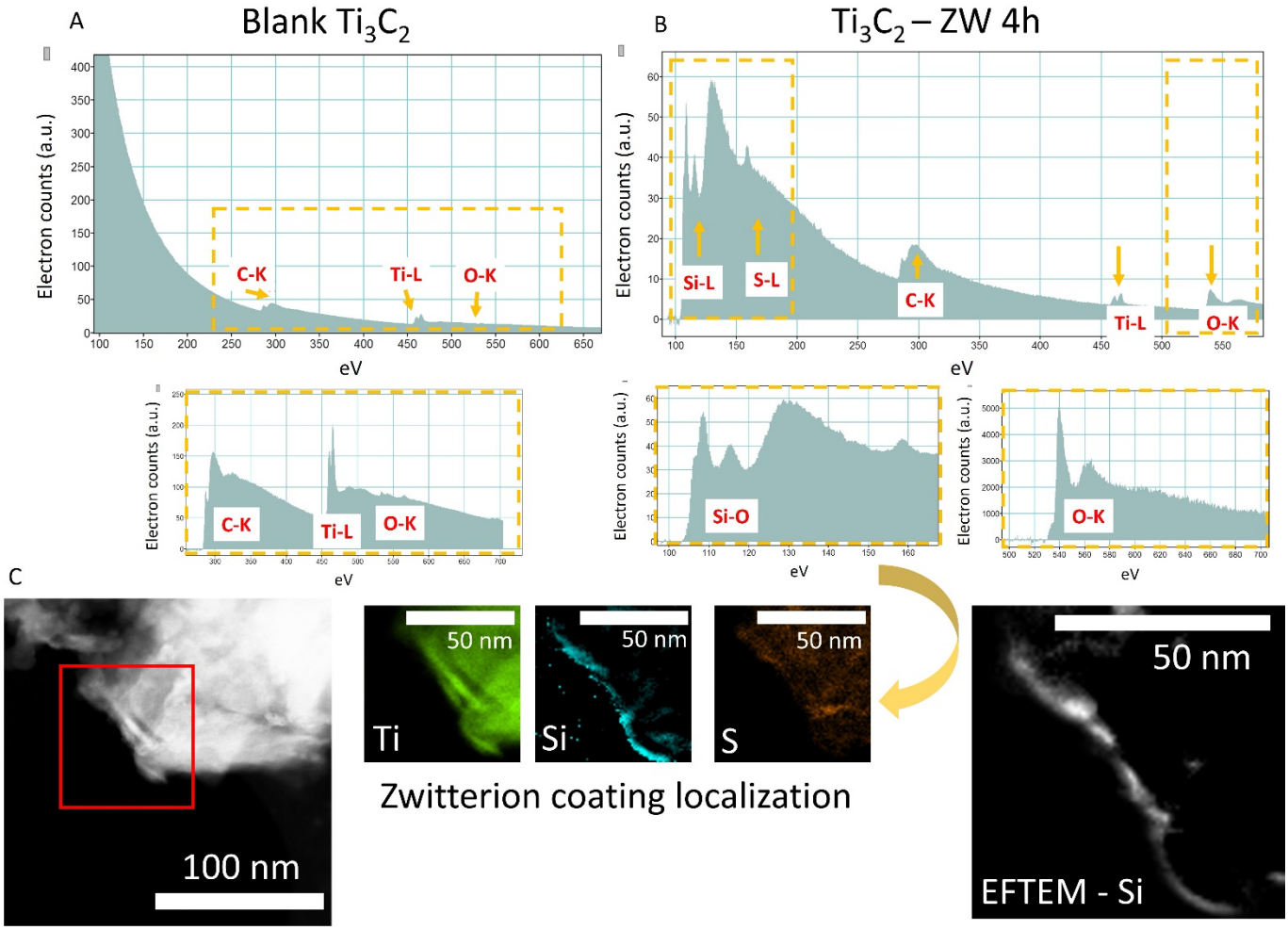

Figure 2. STEM-EELS and STEM-EDS analysis of the composition and binding state of the surface ZW coating: A) An EELS spectrum of the pristine Ti_3C_2; B) An EELS spectrum of the Ti_3C_2-ZW 4h MXene and C) Left: a STEM image of the Ti_3C_2-ZW 4h MXene. The red window shows the area used for STEM-EDS mapping. Middle: STEM -EDS maps showing the localization of the ZW coating at the edge of the material. Right: a STEM-EELS map of Si by using the Si-L EELS signals due to Si-O bonding (as shown in B).

XPS analysis

For a detailed evaluation of the resulted surface change due to coating with zwitterionic molecules (hydrolytic condensation process), XPS spectra of the pristine Ti_3C_2 and modified Ti_3C_2-ZW 4h MXenes are provided (**Figure 3**). As can be seen, a significant component in the O_{1s} spectrum (**Figure 3A1**) at 531.3 eV corresponds primarily to the adsorbed hydroxide on TiO_2 (OH-TiO_2). The surface of the pristine sample also contains small amounts of O_{ad} (peak at 529.1 eV). The C_{1s} HR area (**Figure 3A2**) consists of Ti-C components at 281.5 eV and non-carbide impurities on the surface of the pristine MXene come from the atmosphere and previous reactions. The sp_2, sp_3 bonding and some amount of CH_x component have been observed at 284.2 eV. The C-OH and COO peaks as atmosphere-based contaminants appeared at 285.8 eV and 288.6 eV, respectively. **Figure 3A3** represents the Ti_{2p} HR area with typical key components of Ti_3C_2 MXene. The conclusion is that the Ti_3C_2 surface is mostly terminated with Ti-C, Ti-C-T_o, Ti-C-T_F and TiO_2 components. It is clear that a Ti $2p_{3/2}$ peak at 454.4 eV originates from Ti-C. The other Ti_{2p} features are assigned to Ti atoms that are affected by the F and O occupying sites (Ti-C-T_O and Ti-C-T_F) at 455.2 eV and 456.7 eV respectively for $2p_{3/2}$ signals. The last significant surface termination is realized by TiO_2 components, as is obvious from the $2p_{3/2}$ peak at 458.6 eV.[31]

As obvious from the XPS evaluation, the hydrolytic condensation reaction provides covalently bonded ZW molecules on the Ti_3C_2 MXene surface with thin-film formation (**Figure 3B**). Within C_{1s} the HR area (**Figure 3B1**) of ZW modified samples, a decrease in Ti-C component signal at 281.9 eV has been shown compared to the pristine MXene substrate. As a result of organic coating, dominant signals at 284.6 eV and 285.9 eV belong to C-C and C-OH compounds from the organic coating. The N_{1s} HR area (**Figure 3B2**) consists of three dominant signals for components N-C, N-C=O and -N^+ components at 399.4 eV, 400.2 eV and 401.9 eV, respectively.[32] The spectra of O_{1s} and S_{2p} spectra (**Figure 3B3+4**) suggest the presence of sulfate groups in the form of S=O (-SO^{3-}) at 531.3 eV for O_{1s} and 168 eV for $S_{2p3/2}$, respectively. The hydroxyl functional termination originating from pristine MXene surface and the intermediate step of hydrolytic condensation reaction has appeared at 529.6 eV.[33] The last signal belongs to the Si-O-Si components at 533.3 eV which confirms that the covalent attachment of ZW molecules has been achieved. The Si_{2p} area (**Figure 3B5**) contains a signal at 102.7 eV, which belongs to the Si-O-C or Si-C compounds. Those findings suggest covalent attachment of the surface of MXene, through -Si-OH condensation with hydroxyl-terminated MXene.[34] The Ti_{2p} area (**Figure 3B6**) did not provide any significant change during the ZW coating process and still holds all key signals typical for Ti_3C_2 MXene, such as the components Ti-C, Ti-C-T_O, Ti-C-T_F and TiO_2 components. Elemental ratio evolution has been summarized in **Table 1**. A rapid increase in the organic coating has been observed in the initial step of the reaction. Then, followed by a gradual increase of the key elements for ZW coating, reaches maximal values around 4h and remains almost constant up to 8h reaction.

SEM-EDS analysis

SEM-EDS analysis was performed to i) provide the final 3D design and elemental composition of the electrodes, ii) prove the homogeneous coverage of the elastic carbon fibres with active material and iii) present the morphology stability (**Figure 4**). The carbon cloth substrate is characterized by the smooth surface of individual fibres. The homogeneous surface distribution of carbon and oxygen is in agreement with the appropriate surface chemistry (**Figure 4A+D**). Spray-coated fibres with the pristine Ti_3C_2 active material provide us with homogeneous thin cover throughout the carbon support. Coverage can be proved by the MXene the significant elements such as Ti, O, Al and F in the elemental mapping (**Figure 4B+E**) Similar observation has been seen once carbon fibres were coated with MXene-ZW (**Figure 4C_1+F**), where there is an increase in the signal of representative elements such as Si, N and S. The morphology of the resulting ZW mesoporous layer, formed on the surface of MXene as a smooth film, has been shown in the detailed illustration of **Figure 4C_2** with local protrusions outside the MXene plane (marked with yellow arrows). **Figure 4G** represents the EDS spectra from which the elemental composition is summarized in **Table 2**. Consistent with the XPS findings, we see an increase in ZW significant elements such as O, Si, N and S.

SEM images of the electrodes have been provided before and after 1000 CD cycles. No significant morphological changes have been observed except for the local inorganic clusters of

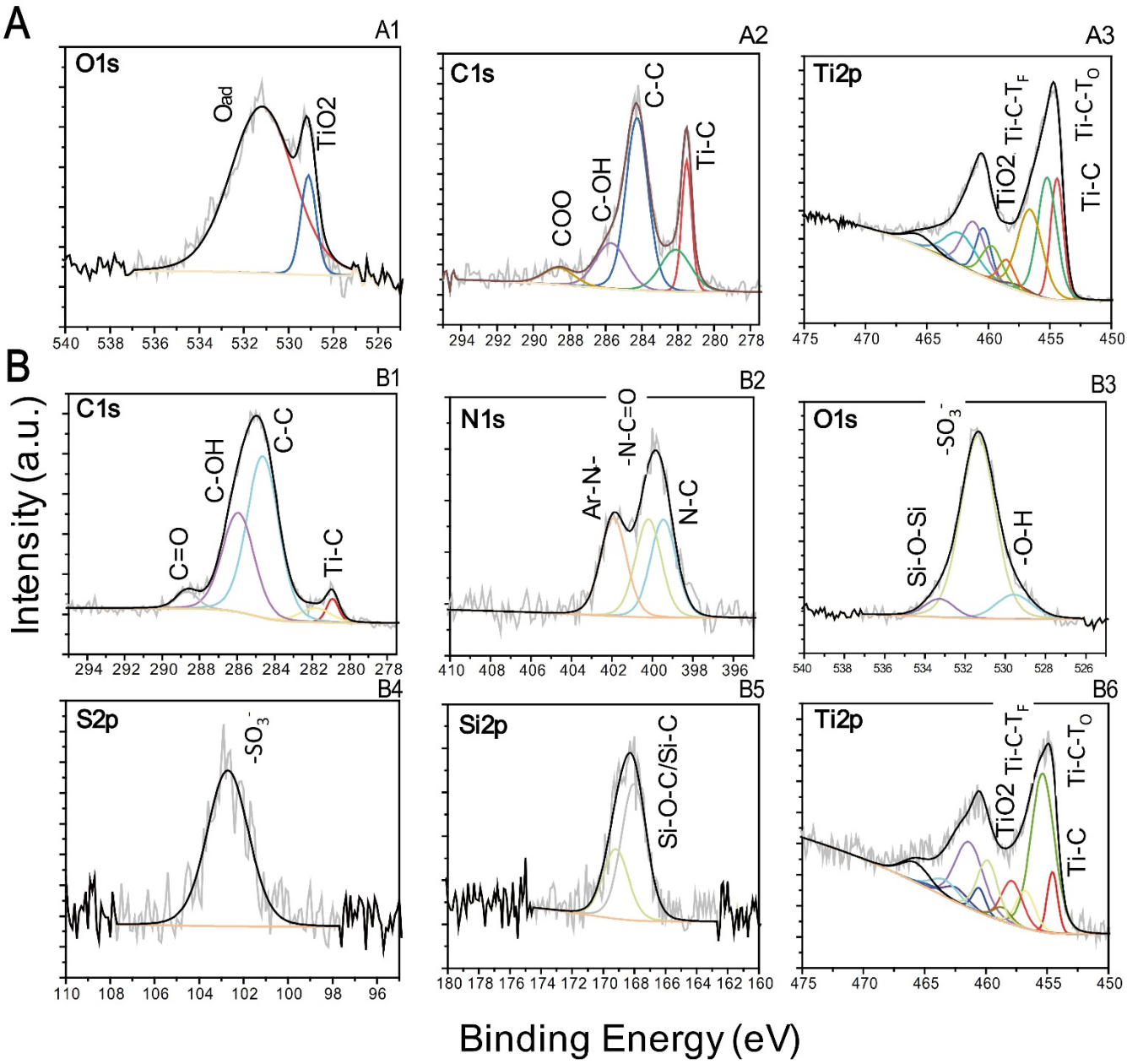

Figure 3. XPS analysis of the pristine Ti_3C_2 MXene and Ti_3C_2-ZW composite after 4h of hydrolytic condensation reaction: A) HR areas (Ti_3C_2) for C 1s, O 1s and Ti 2p; B) HR areas (Ti_3C_2-ZW 4h) for C 1s, O 1s, N 1s, Si 2p, S 2p and Ti 2p.

Table 1. Atomic ration of Ti_3C_2 MXenes as the hydrolytic condensation proceeds.

	Ti	C	O	F	Si	N	S
				at%			
Ti_3C_2	24.65	44.35	15.81	15.19	0	0	0
Ti_3C_2-ZW 1h	9.5	48.5	21.69	21.69	2.92	7.13	2.62
Ti_3C_2-ZW 2h	7.46	49.81	20.31	20.31	3.52	7.12	2.97
Ti_3C_2-ZW 4h	6.63	51.76	20.63	20.63	2.69	7.41	3.44
Ti_3C_2-ZW 8h	6.93	50.08	20.95	20.95	3.63	7.05	3.37

electrolyte-derived ions on the fibre surface (**Figure 4H$_1$+H$_2$** for Ti_3C_2 and Ti_3C_2-ZW4h coated carbon cloths respectively). The corresponding EDS spectra of the electrodes before and after 1000 CD cycles (**Figure 4I)** confirm the expectations in terms of material stability. The same trend has been observed by analysing the morphology and elemental composition of

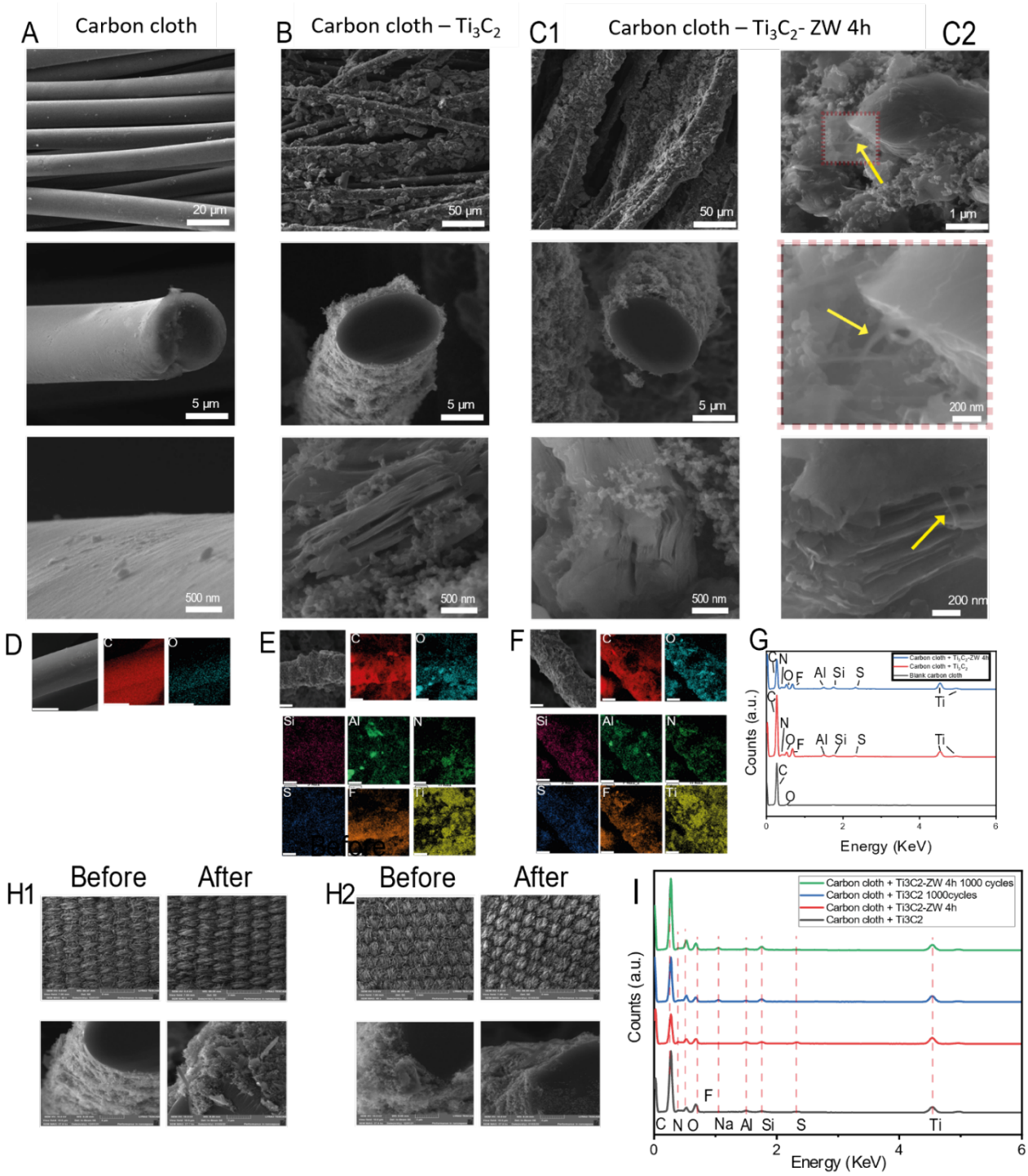

Figure 4. SEM-EDS analysis of the final electrodes coated with MXene-ZW active materials: A+D) Free carbon cloth with corresponding elemental mapping; B+E) Carbon cloth spray-coated with pristine Ti_3C_2 MXene with corresponding elemental mapping; C_1+F) Carbon cloth spray-coated with Ti_3C_2-ZW 4h final composite with corresponding elemental mapping; C_2) Detailed image of the ZW surface coating structure; G) EDS spectra of the carbon cloth, carbon cloth+Ti_3C_2 and carbon cloth with Ti_3C_2-ZW4h; H_1) SEM images of the Ti_3C_2 coated electrodes before and after charge-discharge (CD) 1000 cycles; H_2) SEM images of the Ti_3C_2-ZW 4h coated electrodes before and after 1000 CD cycles; I) EDS spectra of the electrodes before and after 1000 CD cycles.

electrodes prepared using Nb_2C and V_2C MXenes (**Figure S6**).

Table 2. Atomic ration of Ti_3C_2 MXenes on the carbon cloth substrate before and after hydrolytic condensation process.

	Ti	C	O	F	Si	N	S	Si	Al
				(wt %)					
Carbon cloth Ti_3C_2	17.2	66.4	5	10.1	0.6	0	0.5	0.6	0.7
Carbon cloth Ti_3C_2-ZW4h	29.6	46.8	11	9	1.1	0.5	1.5	1.1	1

Electrochemical Performance Analysis

The various MXene substrates (Ti_3C_2, Nb_2C and V_2C) coated with ZW have been used to be tested as a supercapacitor. The electrochemical characterization of the Ti_3C_2-based hybrid has been presented in **Figure 5** (see the supporting information **Figure S7** for the Nb_2C and V_2C based hybrids) including charge-discharge tests, CV tests, EIS – mechanism study, final capacitance evaluation and stability test.

The capacitive behavior of Ti_3C_2//Na_2SO_4//Ti_3C_2 and Ti_3C_2-ZW4h//Na_2SO_4//Ti_3C_2-ZW4h of full devices was evaluated at various scan rates, current densities and operating voltages using symmetric two-electrode cells. The Ti_3C_2-ZW4h//Na_2SO_4//Ti_3C_2-ZW4h device showed excellent electrochemical performance compared to the other devices prepared in this study. **Figure 5A** shows the comparative CV curves of Ti_3C_2//Na_2SO_4//Ti_3C_2 and Ti_3C_2-ZW4h//Na_2SO_4//Ti_3C_2-ZW4h full devices at a scan rate of 100 $mV \cdot s^{-1}$. The area under the CV profile of the Ti_3C_2-ZW4h//Na_2SO_4//Ti_3C_2-ZW4h device is much larger than the Ti_3C_2//Na_2SO_4//Ti_3C_2 device which clearly implies an improvement in electrochemical energy storage. Both devices displayed a rectangular CV curve, which is characteristic of the EDLC-type charge storage mechanism common to carbon-based materials (Ti_3C_2). This mechanism is the result of the used electrolyte (Na_2SO_4), where no any pseudocapacitive behaviour could be find. Both devices exhibited a wide working voltage window, as they could be charged up to 2 V without any overpotential. Similarly, the high polarity and amorphous nature of the Ti3C2-ZW4h electrode material (**Figures 4)** also facilitate the ion diffusion, provide more space for ion storage, and subsequently improve the overall performance of the entire device. In particular, the Ti_3C_2-ZW4h//Na_2SO_4//Ti_3C_2-ZW4h device has exhibited a higher specific capacitance (C_S ~ 35 $F \cdot g^{-1}$) at a scan rate of 10 mVs^{-1} compared to C_S ~ 19 $F \cdot g^{-1}$ for the Ti_3C_2//Na_2SO_4//Ti_3C_2 device at the same scan rate. The higher C_S of the Ti_3C_2-ZW4h//Na_2SO_4//Ti_3C_2-ZW4h device could be attributed to fast ion transport, high conductivity, high polarity and porosity of the electrodes, compared to the Ti_3C_2//Na_2SO_4//Ti_3C_2 device. The structure of zwitterion and charge storage mechanism is shown in **Scheme 2**. **Figure S7-B_2** shows the CV profile of the Ti_3C_2-ZW4h//Na_2SO_4//Ti_3C_2-ZW4h device at various scan rates from 10 to 100 $mV.s^{-1}$. The corresponding CV curves at various scan rates for all devices are shown in **Figure S7-(A_2-F_2)**, respectively. It is noteworthy to mention that even at higher sweep rates, the system retains its rectangular shape and charge storage capability that signifies the stability of Ti_3C_2-ZW4h//Na_2SO_4//Ti_3C_2-ZW4h electrodes.

The improved electrochemical performance of the Ti_3C_2-ZW4h//Na_2SO_4//Ti_3C_2-ZW4h device was further confirmed by GCD studies, as shown in **Figure 5B**. The GCD curves of the Ti_3C_2//Na_2SO_4//Ti_3C_2 and Ti_3C_2-ZW4h//Na_2SO_4//Ti_3C_2-ZW4h devices were compared. As expected for carbon material with an EDLC type charge storing mechanism, a triangular shape was observed in both cases. As a result, the C_S values were determined to be 65.6 $F \cdot g^{-1}$ at 0.07 $A \cdot g^{-1}$ for the Ti_3C_2-ZW4h//Na_2SO_4//Ti_3C_2-ZW4h device while the Ti_3C_2//Na_2SO_4//Ti_3C_2 device registered C_s = 32.6 $F \cdot g^{-1}$ at 0.07 $A.g^{-1}$. The higher C_S of the Ti_3C_2-ZW4h//Na_2SO_4//Ti_3C_2-ZW4h device is attributed to the high polarity, porosity, and conductivity and fast ion transport compared to the other devices. As foreseen, the increase in current density and thickening of the ZW coating decreases C_S, as shown in **Figure 5C** (please see **Figure S7-I** for Nb_2C and V_2C MXenes). The total values of the capacitance are valuable for the neutral electrolyte used in this study (Na_2SO_4). It is also necessary to note that the higher capacitance values could be reached by acidic electrolytes (such as H_2SO_4). However, this is not the goal of this work, where we primarily focus on improving the properties of the given material using a neutral electrolyte. The GCD graphs at various current densities for all devices are shown in the supporting information in **Figure S7-(A_1-F_1)**.

To understand the electrochemical behavior of the electrode materials at the electrode-electrolyte interface, EIS analysis was carried out in a wide frequency region of 100 kHz to 100 mHz with an amplitude of 5 mV (**Figure 5D**). The interfacial resistance results from the Nyquist plot (semicircle diameter in the high-frequency region) and the Warburg impedance (the slope in the low-frequency region). As shown in **Figure 5D**, the Ti_3C_2-ZW4h//Na_2SO_4//Ti_3C_2-ZW4h device showed a smaller semicircle that was designated for the improved electrical conductivity, while the larger semicircle for the Ti_3C_2//Na_2SO_4//Ti_3C_2 device indicates its lower conductivity and is in good agreement with the CV and GDC results, which translated into lower supercapacitor performance. For the high-frequency range, the solution resistance *(R_S)* and the charge-transfer resistance *(R_{CT})* can be obtained from the intercept and the semicircle intercept at the $\acute{Z}_{real}$, respectively. The equivalent series resistance of the Ti_3C_2-ZW4h//Na_2SO_4//Ti_3C_2-ZW4h device is lower (0.8 Ω) than the Ti_3C_2//Na_2SO_4//Ti_3C_2 device (1.2 Ω). On the other hand, the Ti_3C_2-ZW4h//Na_2SO_4//Ti_3C_2-ZW4h device shows a smaller R_{CT} (~16.6

Ω) compared to the Ti_3C_2//Na_2SO_4//Ti_3C_2 device (~17.3 Ω). In summary, the low value of solution resistance and charge-transfer resistance for Ti_3C_2-ZW4h//Na_2SO_4//Ti_3C_2-ZW4h supports the CV and GCD results and suggests its excellent electrochemical behavior (EIS measurements for other devices are provided in the supporting information **Figure S7-G**).

Cycling stability is an essential parameter for evaluating the performance of energy storage devices. At the voltage window of 0-1.5 V, the cycle stability of the Ti_3C_2-ZW4h//Na_2SO_4//Ti_3C_2-ZW4h device is measured at 0.2 $A.g^{-1}$ for 1000 cycles. As demonstrated in **Figure 5E**, the Ti_3C_2-ZW4h//Na_2SO_4//Ti_3C_2-ZW4h device possesses an initial capacitance of 37.5 $F.g^{-1}$ and maintains 34.3 $F.g^{-1}$ after 1000 cycles at 0.2 $A.g^{-1}$ (approx. 92% of capacitance retention), implying outstanding cycle stability Interestingly, investigation of the electrochemical stability of the full device at the current density of 0.2 $A \cdot g^{-1}$ showed that the Ti_3C_2-ZW4h//Na_2SO_4//Ti_3C_2-ZW4h device has a great potential for higher energy storage applications in the studied potential window.

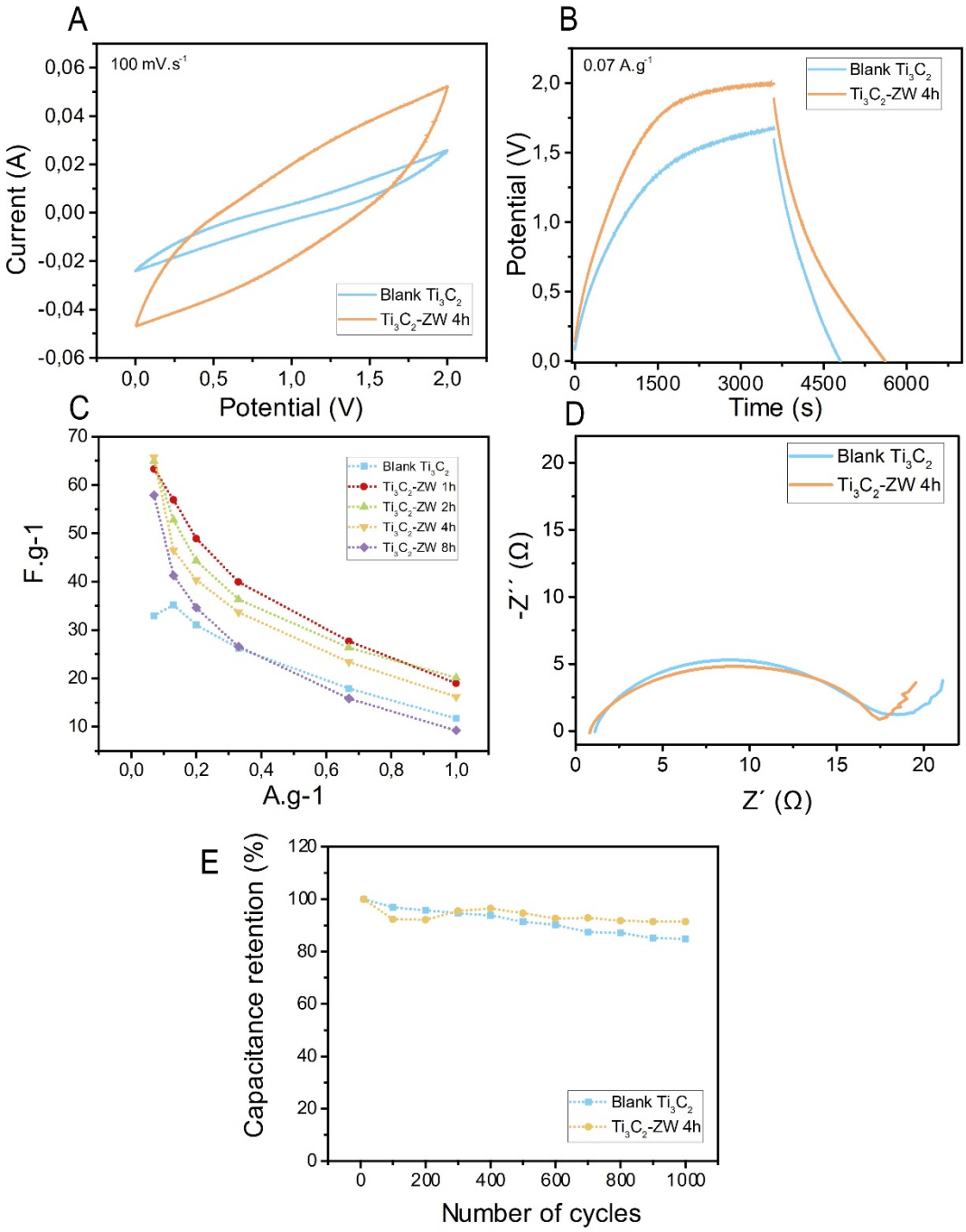

Figure 5. A) Comparison of the cyclic voltammogram (CV); and B) Comparison of galvanostatic charge-discharge (GCD); C) Calculated CS of Ti_3C_2//Na_2SO_4//Ti_3C_2 and Ti_3C_2-ZW//Na_2SO_4//Ti_3C_2-ZW 4h full devices at various current densities and various ZW densities; D) EIS graph of Ti_3C_2//Na_2SO_4//Ti_3C_2 and Ti_3C_2-ZW4h//Na_2SO_4//Ti_3C_2-ZW4h full devices; E) CS retention versus number of cycles for Ti_3C_2//Na_2SO_4//Ti_3C_2 and Ti_3C_2-ZW4h//Na_2SO_4// Ti_3C_2-ZW4h at 0,2 $A.g^{-1}$.

Conclusion

In summary, a 3D structured electrode has been designed via an MXene-organic hybrid approach as a facile, versatile and effective strategy. Various MXene substrates (Ti_3C_2, Nb_2C and V_2C) are coated with zwitterions. Various characterization techniques have been employed to confirm the successful, covalent immobilization of ZW molecules into the MXene-organic hybrid. The gradual increase in ZW density on the surface as a function of the hydrolytic condensation reaction time (1, 2, 4 and 8 hours) has also been studied and proved. Although ZW preserves the original instinct property of the MXenes, the electrochemical storage properties of Mxene-ZW increase significantly as a result of the reactivity of the charged organic molecules. Moreover, mesoporous -Si-O-Si- forms a passivation layer that notably enhances stability. All prepared MXene-ZW

hybrids have been tested in a full device and compared. It is noteworthy that the Ti_3C_2-ZW4h//Na_2SO_4//Ti_3C_2-ZW4h device has the best performance (66 $F.g^{-1}$, at 0.07 $A.g^{-1}$). The improved performance of the MXene-ZW hybrids arising from the high polarity and amorphous nature of the hybrid electrode material facilitates the ion diffusion, provides more space for ions storage, and subsequently improves the overall performance of the full device. The fabricated electrode retains 92% of the capacitance after 1000 cycles at 0.2 $A.g^{-1}$. This work presents a versatile approach to designing MXene-based hybrid electrodes with high-performance and stable pseudocapacitive behavior. To the best of the author's knowledge, more than 20 different MXene compositions have been reported, and many more have been predicted theoretically. This study opens a new route to designing hybrid materials based on MXenes for the design and fabrication of high-performance supercapacitors. Moreover, ZW coatings apply to a wide range of MXene-based substrates. Main Text Paragraph.

Experimental Section

Essential Experimental Procedures/Data. ((All other characterization data, original spectra, etc., should be provided in the Supporting Information))

Acknowledgements

This work was supported by Czech Science Foundation (GACR No. 20-16124J) and the Knut and Alice Wallenberg Foundation (2019.0140). This project has received funding from the European Union's Horizon 2020 research and innovation programme under grant agreement No 823717 – ESTEEM3. This work was performed in part at the Chalmers Material Analysis Laboratory, CMAL.

Keywords: Supercapacitor, 2D materials, MXenes, Organic molecules

[1] Patrice Simon, Yury Gogotsi, *Nature Materials* **2008**, *7*, 845–854.
[2] a) Qiu Jiang, Narendra Kurra, Mohamed Alhabeb, Yury Gogotsi, Husam N. Alshareef, *Adv. Energy Mater* **2018**, *8*; b) Yury Gogotsi, *Nature* **2014**, *509*, 568–569.
[3] Veronica Augustyn, Patrice Simonb, Bruce Dunn, *Energy Environ. Sci.* **2014**, *7*, 1597–1614.
[4] Jinbo Pang, Rafael G. Mendes, Alicja Bachmatiuk, Liang Zhao, Huy Q. Ta, Thomas Gemming, Hong Liu, Zhongfan Liu, Mark H. Rummeli, *Chem. Soc. Rev* **2019**, *48*, 72--133.
[5] YOICHI KUBOTA, KENJI WATANABE, OSAMU TSUDA, TAKASHI TANIGUCHI, *SCIENCE* **2007**, *317*, 932-934.
[6] Manish Chhowalla, Hyeon Suk Shin, Goki Eda, Lain-Jong Li, Kian Ping Loh, Hua Zhang, *Nature Chemistry* **2013**, *5*, 263–275.
[7] Boubekeur Lalmi, Hamid Oughaddou, Hanna Enriquez, Abdelkader Kara, Sébastien Vizzini, Bénidicte Ealet, Bernard Aufray, *Appl. Phys. Lett.* **2010**, *97*.
[8] Elisabeth Bianco, Sheneve Butler, Shishi Jiang, Oscar D. Restrepo, Wolfgang Windl, Joshua E. Goldberger, *ACS Nano* **2013**, *7*, 4414–4421.
[9] Johan E. ten Elshof, Huiyu Yuan, Pablo Gonzalez Rodriguez, *Adv. Energy Mater.* **2016**, *6*.
[10] Ke Li, Meiying Liang, Hao Wang, Xuehang Wang, Yanshan Huang, João Coelho, Sergio Pinilla, Yonglai Zhang, Fangwei Qi, Valeria Nicolosi, Yuxi Xu, *Adv. Funct. Mater* **2020**, *30*.
[11] Maria R. Lukatskaya, Sankalp Kota, Zifeng Lin, Meng-Qiang Zhao, Netanel Shpigel, Mikhael D. Levi, Joseph Halim, Pierre-Louis Taberna, Michel W. Barsoum, Patrice Simon, Yury Gogotsi, *Nature Energy* **2017**, *2*.
[12] Babak Anasori, Maria R. Lukatskaya, Yury Gogotsi, *Nature Reviews Materials* **2017**, *2*.
[13] Michael Naguib, Murat Kurtoglu, Volker Presser, Jun Lu, Junjie Niu, Min Heon, Lars Hultman, Yury Gogotsi, Michel W. Barsoum, *Advanced Materials* **2011**, *23*, 4248-4253.
[14] MARIA R. LUKATSKAYA, OLHA MASHTALIR, CHANG E. REN, YOHAN DALL'AGNESE, PATRICK ROZIER, PIERRE LOUIS TABERNA, MICHAEL NAGUIB, PATRICE SIMON, MICHEL W. BARSOUM, YURY GOGOTSI, *SCIENCE* **2013**, *341*, 1502-1505.
[15] Mengzhou Yua, Si Zhoub, Zhiyu Wanga, Jijun Zhaob, Jieshan Qiua, *Nano Energy* **2018**, *44*, 181-190.
[16] a) Xianfen Wang, Satoshi Kajiyama, Hiroki Iinuma, Eiji Hosono, Shinji Oro, Isamu Moriguchi, Masashi Okubo, Atsuo Yamada, *Nature Communications* **2015**, *6*; b) Satoshi Kajiyama, Lucie Szabova, Hiroki Iinuma, Akira Sugahara, Kazuma Gotoh, Keitaro Sodeyama, Yoshitaka Tateyama, Masashi Okubo, Atsuo Yamada, *Advanced Energy Materials* **2017**, *7*.
[17] Mohamed Alhabeb, Kathleen Maleski, Babak Anasori, Pavel Lelyukh, Leah Clark, Saleesha Sin, Yury Gogotsi, *Chem. Mater.* **2017**, *29*, 7633–7644.
[18] Narendra Kurra, Bilal Ahmed, Yury Gogotsi, Husam N. Alshareef, *Adv. Energy Mater* **2016**, *6*.
[19] Tingting Tu, Bo Liang, Shanshan Zhang, Tianyu Li, Bin Zhang, Shiyi Xu, Xiyu Mao, Yu Cai, Lu Fang, Xuesong Ye, *Adv. Funct. Mater* **2021**, *31*.
[20] Jianmin Luo, Wenkui Zhang, Huadong Yuan, Chengbin Jin, Liyuan Zhang, Hui Huang, Chu Liang, Yang Xia, Jun Zhang, Yongping Gan, Xinyong Tao, *ACS Nano* **2017**, *11*, 2459–2469.
[21] R. Garg, A. Agarwal, M. Agarwal, *Journal of Materials Science: Materials in Electronics* **2021**, *32*, 22046–22059.
[22] Aristides Bakandritsos, Demetrios D. Chronopoulos, Petr Jakubec, Martin Pykal, Klára Cepe, Theodore Steriotis, Sergii Kalytchuk, Martin Petr, Radek Zboril, Michal Otyepka, *Adv. Funct. Mater* **2018**, *28*.
[23] Sehyeong Lim, Hyunsu Park, Jin Hyung Kim, Jeewon Yang, Chaesu Kwak, Jieun Kim, Seoung Young Ryu, Joohyung Lee, *RSC Adv.* **2020**, *10*, 25966–25978.
[24] Cheng-Feng Du, Xiangyuan Zhao, Zijiao Wang, Hong Yu, Qian Ye, *Nanomaterials* **2021**, *11*.
[25] Rui Liu, Weihua Li, *ACS Omega* **2018**, *3*, 2609−2617.
[26] Kanthasamy Raagulan, Ramanaskanda Braveenth, Bo Mi Kim, Kwang Jin Lim, Sang Bok Lee, Miyoung Kim, Kyu Yun Chai, *RSC Adv.* **2020**, *10*, 1613–1633.
[27] Tomasz Cygan, Jaroslaw Wozniak, Mateusz Petrus, Artur Lachowski, Wojciech Pawlak, Bogusława Adamczyk-Cieślak, Agnieszka Jastrzębska, Anita Rozmysłowska-Wojciechowska, Tomasz Wojciechowski, Wanda Ziemkowska, Andrzej Olszyna, *Materials* **2021**, *14*.
[28] a) Mani Manivannan, Susai Rajendran, *International Journal of Engineering Science and Technology* **2011**, *3*, 8048-8060; b) Mehrnoush Mokhtarimehr, Mahmoud Pakshir, Akbar Eshaghi, Mohammad Hossien Shariat, *Thin Solid Films* **2013**, *532*, 123–126.
[29] Xin Qian, Xuefei Wang, Junjun Zhong, Jianhai Zhi, Fangfang Heng, Yonggang Zhang, Shulin Song, *J Raman Spectrosc.* **2019**, *50*, 665–673.
[30] Ruiyang Kang, Zhenyu Zhang, Liangchao Guo, Junfeng Cui, Yapeng Chen, Xiao Hou, Bo Wang, Cheng-Te Lin, Nan Jiang, Jinhong Yu, *Scientific Reports* **2019**, *9*.
[31] Lars-Åke Näslund, Per O. Å. Persson, Johanna Rosen, *J. Phys. Chem. C* **2020**, *124*, 27732–27742.
[32] G. P. Syed Ibrahim, Arun M. Isloor, Inamuddin, Abdullah M. Asiri, Norafqah Ismail, Ahmed Fauzi Ismail, Ghulam Md Ashraf, *Scientific Reports* **2017**, *7*.

[33] Zachary D.Hood, Shiba P.Adhikari, Samuel F.Evans, Hui Wang, Yunchao Li, Amit K.Naskar, Miaofang Chi, Abdou Lachgar, M. Parans Paranthaman, *Carbon Resources Conversion* **2018**, *1*, 165–173.

[34] Mohammed Abdelhameed, Shawkat Aly, Jeremy T. Lant, Xiaoran Zhang, Paul Charpentier, *Scientific Reports* **2018**, *8*.